

**IMAGE RECONSTRUCTION FOR
IMAGING SYSTEMS WITH
CIRCULAR SYMMETRIC OBSERVATION**

Michael Y. Jin

Jet Propulsion Laboratory
California Institute of Technology
Pasadena, California 91109, USA

PHONE: (818) 354-3778

TELEFAX: (818) 393-6943

E-MAIL: michael_jin@radar-email.jpl.nasa.gov

The research described in this paper was carried out by the Jet Propulsion Laboratory, California Institute of Technology, under a Contract with the National Aeronautics and Space Administration.

Abstract

A new image reconstruction algorithm for imaging systems with circular symmetric observation is presented in this paper. Typical imaging systems of this kind include the holographic synthetic aperture radar (HSAR), the computer aided tomography (CAT), and the ultrasonic reflectivity tomography (URT). Based on the circular symmetry, this algorithm performs fast Fourier correlation in the azimuth dimension. The reference functions are the amplitude weighted two-dimensional spectra of the point target responses (PTR). The reference function is updated for each range bin to achieve exact focusing. By choosing proper weighting functions, this algorithm is capable of generating an ideal point spread function as that predicted by the Fraunhofer diffraction of a circular aperture. The computation efficiency of this algorithm is one order of magnitude better than the convolution backprojection algorithm due to the characteristics of the 2-D spectrum of the PTR.

1. INTRODUCTION

The problem of image reconstruction for imaging systems with circular symmetric observations is considered in this paper. In this type of systems, observation of the targets is made by sensors located at points equally spaced around a circle surrounding the targets. Each observation results in a stream of data samples, each of which is the line integral of the target signature. A broad range of imaging systems falling into this category can be found in the fields of synthetic aperture radar (SAR), the computer aided tomography (CAT), the ultrasonic imaging, and sonar. In the SAR field, this type systems include the holographic SAR (HSAR) [1, 2] in a circular flight path and the inverse SAR (ISAR) [3]. In the CAT field, they include x-ray CAT systems, both parallel beam and fan beam [4], the magnetic resonance imaging (MRI) system [5], and the positron emission tomography (PET) system [6]. In the ultrasonic imaging field, it includes the ultrasonic reflectivity tomography (URT) [7]. In this paper, four imaging systems are chosen as examples for analysis. These are the holographic synthetic aperture radar (HSAR), the x-ray computer aided tomography (CAT), both parallel beam and fan beam, and the ultrasonic reflectivity tomography (URT). The analysis given in this paper, however, will be applicable to all the above mentioned imaging systems.

A HSAR in a circular path is shown in Figure 1a. In this system, an aircraft flies along a circular flight path above the ground. Its wide beam radar points to the center of

the flight circle. Electromagnetic pulses are transmitted periodically from the radar to the ground. These signals are bounced back from the ground targets, within the radar footprint, and received by the same radar. Echo signals are then demodulated by the carrier frequency, converted into discrete data samples, and processed into images in real time or stored in an on-board recorder for later processing.

The geometry of a two dimensional ultrasonic reflectivity tomography is depicted in Figure 1b. It consists of a water tank of dimensions greater than that of the object to be imaged. A moving transducer with a very narrow beam width in the third dimension scans over the outer circle. Ultrasonic pulses are emitted from the transducer. Signals reflected from the imaged object are sensed by a receiver, collocated with the transducer, for further processing. For simplification, we shall consider that the object is an idealized reflecting medium in which the velocity of the sound is constant, the medium is weakly reflecting, and absorption is uniform over the region of interest [7].

The first and second generation x-ray CAT systems are shown in Figure 2a. In this configuration, the x-ray source generates parallel x-ray beams. The x-ray sensors are aligned perpendicular to these x-ray beams for detecting x-rays passing through the imaged object. These detected signals represents the projection of the object from all different view angles. The third and fourth generation x-ray CAT systems [8] are using fan beams as shown in Figure 2b. In this configuration, the point source generates x-ray beams in radial directions. The stationary x-ray sensors are mounted on an outer circle. Since the detected signals does not represent the projection of the object of any view angle, image reconstruction algorithm is generally different.

Differences among the systems illustrated in Figure 1 and 2 can be summarized as follows. The detected signal of the x-ray CAT is the logarithm of the attenuation of the target. The received signals from the HSAR and URT systems are the back scatter of the electromagnetic (EM) wave and ultrasonic wave, respectively. Figure 3 illustrates the geometry's of the lines, along which the target signatures are superposed and detected by the sensors. In the CAT systems, these lines are straight ones. The spacing between these lines is determined by the width of the x-ray beams. In both HSAR and URT, the lines are concentric circles. The spacing between these lines is determined by the width of the effective radar impulse or the effective ultrasonic impulse. For the HSAR, an addition factor affecting the line spacing is the local incidence angle of the EM wave.

1.1 History of Processing Algorithms

The mathematical foundations of tomography was established by Radon [9]. The development of the CAT in medical applications started at early 70 and has been stabilized after two decades. Except the once used iterative algebraic reconstruction algorithm [10], commonly used image reconstruction algorithms include the convolution backprojection (CBP) [11, 12] and the direct Fourier method [13]. The CBP algorithm is most popular in CAT image reconstruction because of its better image quality and easy adaptation to the fan beam geometry. The direct Fourier algorithm is highly efficient in computation. However, its image quality highly depends on the type and length of the interpolator used to covert signal spectrum into a Cartesian grid. In addition, its application is limited to the parallel beam CAT.

The concept of the synthetic aperture radar was pioneered by Carl Wiley of the Goodyear Aircraft Company. Image reconstruction based on Doppler processing are widely used in the SAR processing field [14,15,16,17]. The analogy between the parallel beam CAT and a coherent imaging system for observing a rotating object was first reported by Mensa [18]. Later this analogy was extended to the SAR and the spotlight SAR [19]. Since then, both the CBP and direct Fourier algorithms were successfully applied to the SAR applications [20, 21]. Again, the CBP algorithm yields better image quality than the direct Fourier algorithm. Another algorithm needs to be mentioned is the circular convolution algorithm applied to the coherent Doppler tomography (CDT) [22, 23]. When dealing with systems using CW irradiation, this algorithm was found both efficient and with high image quality.

The SAR related systems mentioned above were mostly confined to a narrow radar beam and a narrow signal bandwidth as compared to the radar carrier frequency. In addition, most analysis has been made to the far field problem such that the iso-range lines may be approximated by parallel lines. Recent development in foliage and ground penetration radar employs radars with longer wavelengths. Due to the limitation of the antenna size, the radar beam angle naturally becomes much wider. Furthermore, in order to achieve a high resolution, as compared to its wavelength, the signal bandwidth must also be wide as compared to its carrier or center frequency. System of this kind may be referred to as the holographic SAR (HSAR) [3]. Examples of this type radar system include those developed in Sweden's National Defense Research Establishment [24] and SRI International [25]. In this field, the image reconstruction algorithm is still in its early

development stage. This also gives the motivation of this paper to develop algorithm applicable to this area.

Most popular ultrasonic medical imaging systems used in diagnosis include the B scan imaging mode and transducer arrays [9]. The B scan mode image is obtained by spatially scanning a pencil beam ultrasonic device along the surface of an object. The image of a cross section of the object is the reflected signal displayed as a two-dimensional function of time and scanning distance. The transducer arrays allows the ultrasonic beam steered to any direction in a plane to avoid the need of moving the transducer as that in the B scan mode. Other imaging modes still in experimental or study stage include the ultrasonic transmission tomography [26], the ultrasonic reflectivity tomography [27, 2], and the ultrasonic diffraction tomography [28]. The problem addressed in [7] is of particular interest. This is because that its problem formulation using line integrals is analogous to that used in the CAT system, but, the nature of wave phenomena is analogous to a SAR system. The algorithm proposed in [7] is an exact solution based on Hankel transforms. A shortcoming of this algorithm is that it is very difficult to implement the Hankel transform for both high accuracy and efficient computation.

2. IMAGE RECONSTRUCTION USING PTRSPECTRUM

In this section, the point target responses of several imaging systems are formulated. The data received by the imaging system is expressed in terms of both the target signature and the point target response. The image reconstruction algorithm is then described.

To illustrate the concept of image reconstruction based on the point target response (PTR), let us consider an ideal case radar system: a pencil beam radar as shown in Figure 4. In this system, the width of the radar beam is such that its azimuth spatial resolution is equal to its range resolution. The data gathered by this radar in one complete observation cycle directly represents the target image in a polar grid. Other than an interpolation process to convert data samples back to the Cartesian grid, no image reconstruction process is required. Obviously, in such a system, a single point target within the imaging circle would cause a single point-like response among all observed data. This point-like response is usually referred to as the point spread function (PSF). In contrast, a point target imaged by a wide beam HSAR will cause a line-like response in the observed data set as shown in Figure 7c. This line-like PTR may be viewed as a “blurred” version of the PSF. Therefore,

one may utilize the concept of inverse filtering [30] to restore the resolution for the image concealed in the observed data.

To extend the PTR concept to the CAT systems, one must introduce the idea of the data reference point and equivalent distance. Figure 5a and 5b illustrates the geometry of the distance r_{st} between the target and the radar sensor or ultrasonic transducer. In contrast, Figure 5c and 5d illustrates the geometry of the equivalent distance r_{st} between the target and the data reference point. The data reference point is defined as the point lying on the imaging circle encircling all the imaged area and the line connecting the data reference point and the center of the circle must be perpendicular to the x-ray beam passing the center. In polar coordinate, let (r_s, θ) represent the coordinate of the sensor or data reference point, where the origin of the coordinate is the center of the circle and θ is referred to as the azimuth angle of the sensor. (r_t, φ) represents the Coordinate Of a Point target, the distance or equivalent distance of four example systems can be expressed by:

(1) Computer Aided Tomography - Parallel Beam

$$r_{st}(\theta) = r_{st}(\theta, r_t, \varphi) = r_s - r_t \cdot \cos(\varphi - \theta) \quad (1)$$

(2) Computer Aided Tomography - Fan Beam

$$r_{st}(\theta) = r_s - \frac{r_s}{\tan \gamma} \cdot \frac{r_t \cdot \cos(\varphi - \theta)}{(r_s / \tan \gamma) - r_t \cdot \sin(\varphi - \theta)} \quad (2)$$

where γ is the half angle of the x-ray fan beam as shown in Figure 3.d.

(3) Ultrasonic Reflective Tomography

$$r_{st}(\theta) = \sqrt{r_s^2 + r_t^2 - 2r_s r_t \cdot \cos(\varphi - \theta)} \quad (3)$$

(4) Holographic Synthetic Aperture Radar

$$r_{st}(\theta) = \sqrt{h^2 + r_s^2 + r_t^2 - 2r_s r_t \cdot \cos(\varphi - \theta)} \quad (4)$$

where h is the altitude of the aircraft in Figure 3a. Eq. (4) differs from Eq. (3) only by the radar altitude. When h approaches zero, Eq. (4) approaches Eq. (3). In the following sections, the analysis for the URT and HSAR systems will be combined when there is no need for making a distinction. In the fan beam CAT, the range of the target r_t must be within $r_s \cos \gamma$ in order to be illuminated in all angles.

In a SAR system, the point target response from a impulse like radar pulse can be expressed as the same impulse with a time delay associated with its round-trip wave traveling distance. For a point target located at (r_t, φ) with a physical dimension much smaller than the width of the radar impulse, its response is given by

$$P_{(r_t, \varphi)}(t, e) = \delta(t - \frac{2 \cdot r_{st}(\theta, r_t, \varphi)}{c}) \quad \text{for } 0 \leq \theta \leq 2\pi \quad (5)$$

where c is the speed of light and $\delta(t)$ is a delta function. Here, the Doppler frequency introduced by the relative velocity between the radar and the target is ignored since it is a reasonable approximation for most cases. Also, the motion error associated with a HSAR is not considered in the following analysis. By changing the time coordinate into a spatial coordinate with $t = (2 \cdot r_d) / c$, we can rewrite the point target response as

$$P_{(r_t, \varphi)}(r_d, \theta) = \delta(r_d - r_{st}(\theta, r_t, \varphi)) \quad \text{for } 0 \leq \theta \leq 2\pi \text{ and } 0 \leq r_d \leq 2r_s \quad (6)$$

It is more convenient to reverse the sequence of the data samples and shift the reference point to that corresponding to the center of the imaging circle by choosing a variable $r = r_{shift} - r_d$, where r_{shift} is equal to r_s for both CAT systems and the URT system, and r_{shift} is equal to $\sqrt{r_s^2 + h^2}$ for the HSAR system. Then Eq. (6) can be expressed as

$$P_{(r_t, \varphi)}(r, \theta) = \delta(r - r_{ot}(\theta, r_t, \varphi)) \quad \text{for } 0 \leq \theta \leq 2\pi \text{ and } -r_s \leq r \leq r_s \quad (7)$$

where $r_{ot}(e, r_t, \varphi) = r_{shift} - r_{st}(\theta, r_t, \varphi)$. For a SAR system with limited bandwidth centered at a carrier frequency f_c , its delta function can be expressed by the summation of two terms, each corresponding to one segment of the spectrum shown in Figure 6a.

$$\delta(r - r') = \frac{\sin(\pi \cdot (r - r') / \delta r)}{(\pi \cdot (r - r') / \delta r)} \cdot (\exp\{-j2\pi \frac{r'}{\lambda / 2}\} + \exp\{j2\pi \frac{r'}{\lambda / 2}\}) \quad (8a)$$

where λ is associated with the carrier frequency, $\delta r = c / (2 B_r)$ is the range resolution, c is the speed of light, and B_r is the bandwidth of the radar. For a wide band radar with its pulse spectrum shown in Figure 6b, the radar bandwidth is twice the radar center frequency such that the two sidebands joint at the origin of the spectrum. In this case, the effective radar bandwidth is doubled such that the range resolution is equivalent to one eighth of the wavelength of the carrier frequency, i.e. $\delta r = \lambda / 8$, since the relationship

between the carrier frequency and the total band width B_r is given by $f_c = B_r / Q$. For such a system, its associated delta function is simply

$$\delta(r - r') = \frac{\sin(\pi \cdot (r - r') / \delta r)}{(\pi \cdot (r - r') / \delta r)} \quad (8b)$$

Unless pointed out, the analysis throughout this paper will be based on the wide band, low carrier frequency case as shown Figure 6b.

For the URT system, all formulation for the point target response are applicable except that c must be replaced by the speed of the ultrasonic wave in the imaging object. For the parallel beam CAT system, only equations (6) and (7) are applicable. The range resolution δr is determined by the width of the x ray beam and the intensity distribution of the x-ray within the beam. For simplicity, a $\sin x / x$ function is also used for the following analysis on the CAT systems. For the fan beam CAT system, the range resolution in Eq. (8) must modified to take into account the effect due to the varying distance from the target to the x-ray source . Again, this effect is not considered in this paper for simplicity.

Plots of these point target response are given in Figure 7. These curves can be viewed as the superposition of a large number of short line segments, each with a different slope. Since the two-dimensional Fourier transform of a line with slope s , length L , and width D is another line with slope $-s^*$, length D^{-1} and width L^{-1} , one can see that the energy distribution of the 2-D spectrum of these point target response covers a very large area. This indicates that high resolution image can be reconstructed by means of proper filtering such as inverse filter or complex conjugate filter. Detailed analysis for the 2-D spectrum of the PTR is given in Section 3. It can also be seen that in both 7a and 7b the upper line segment is symmetric to the lower line segment. This implies that only one half of the PTR is require for constructing image with a full resolution.

Based on circular symmetry, the data received by the sensor can be written as the range integral of the azimuth convolution of the target signature with the point target response.

$$\begin{aligned} E(r, \theta) &= \iint \sigma(r_t, \varphi) * P_{(r_t, \varphi)}(r, \theta) \cdot dr_t d\varphi \\ &= \iint \sigma(r_t, \varphi) \cdot \delta(r - r_{ot}(\theta, r_t, \varphi)) \cdot dr_t d\varphi \end{aligned} \quad (9)$$

The circular convolution algorithm described in [22] is modified hereby utilizing the 2-D spectrum of the PTR as the reference function. Since the images obtained from [22] and the proposed algorithm are in a polar coordinate, further interpolation is required to convert them to a Cartesian coordinate. The image quality degradation due to this interpolation is less severe than the interpolator used for converting the coordinate of the spectrum [13]. This point will be illustrated furthermore in Section 8.

The basic equation for image reconstruction using PTR approach can be expressed by the range frequency integration of the inverse azimuth transform of the product of two dimensional spectrum of the received data and a reference function

$$\sigma(r, \theta) = \iint E(R, \Theta) \cdot Ref_r^*(R, \Theta) \cdot e^{j2\pi\theta\Theta} \cdot dR d\Theta \quad (10)$$

where $*$ denote complex conjugate operation, R is the range spatial frequency, Θ is the azimuth angular frequency, $E(R, \Theta)$ is the two dimensional spectrum of the received data, and $Ref_r(R, \Theta)$ is the reference function for image reconstruction. Since the reference function is r dependent, therefore, it needs to be updated for processing each image line. The reference function is given by the product of an amplitude weighting function and the two dimensional spectrum of the point target response of a point located at (r, θ) .

$$Ref_r(R, \Theta) = W_r(R, \Theta) \cdot \iint \delta(r' - r_{ot}(\theta', r, \theta)) \cdot e^{-j2\pi r'R} \cdot e^{-j2\pi \theta'\Theta} dr' d\theta' \quad (11)$$

where $W_r(R, \Theta)$ is the weighting function used to control the shape of the PSF of each point target in order to meet the requirement for certain image application.

3. TWO-DIMENSIONAL SPECTRUM OF THE PTR

Recent advancement in spaceborne SAR data processing utilizes the wave domain approach [29,30]. The advantage of this approach is that it gives the exact solution to the reconstruction problem. Its point spread function approaches the theoretical predicted function. For the problem addressed in this paper, the 2-D spectrum of a PTR for a point target located at (r, θ) can be expressed as

$$E_{pt}(R, \Theta) = \iint \delta(r' - r_{ot}(\theta', r, \theta)) \cdot e^{-j2\pi r'R} \cdot e^{-j2\pi \theta'\Theta} dr' d\theta' \quad (12)$$

By eliminating the delta function, we have

$$E_{pt}(l?, @) = \int e^{-j2\pi r_{ot}(\theta', r, \theta)R} \cdot e^{-j2\pi \theta' \Theta} dr' d\theta' \quad (13)$$

This is the Fourier transform of a frequency modulation signal. The approximation form of the 2-D spectrum can be obtained by using the stationary phase principle [32]. Before getting the Fourier transform, let us rewrite Eq. (12) as the summation of the Fourier transforms of two segments of the frequency modulation signal.

$$E_{pt}(R, \Theta) = \int_{\theta_1}^{\theta_2} e^{-j2\pi r_{ot}(\theta', r, \theta)R} \cdot e^{-j2\pi \theta' \Theta} dr' d\theta' + \int_{\theta_2}^{\theta_1} e^{-j2\pi r_{ot}(\theta', r, \theta)R} \cdot e^{-j2\pi \theta' \Theta} dr' d\theta' \quad (14)$$

These two segments of frequency modulation signals are characterized by their opposite signs in the second order derivative of $r_{ot}(\theta', r, \theta)$. θ_1 and θ_2 are the boundary points between these two segments. The Fourier transform of Eq. (12) can be expressed by

$$E_{pt}(l?, @) = A_1(R, \Theta) \cdot e^{j\Phi_1(R, \Theta)} + A_2(R, \Theta) \cdot e^{j\Phi_2(R, \Theta)} \quad (15)$$

where

$$A_i(R, \Theta) = \sqrt{2\pi} \left| \frac{d^2(-R \cdot r_{ot}(\theta))}{d\theta^2} \right|_{\theta=\theta_0}^{-1/2}, \quad (16)$$

and

$$\Phi_i(R, \Theta) = 2\pi(-\Theta \cdot \theta_0 - R \cdot r_{ot}(\theta_0)) - \text{sgn}\left[\frac{d^2 r_{ot}(\theta', r, \theta_0)}{d\theta^2}\right] \frac{\pi}{2} \quad (17)$$

$\text{sgn}[\cdot]$ is the sign function and θ_0 is the stationary-phase point given by the solution of the following equation

$$2\pi \frac{d(-\Theta \cdot \theta - R \cdot 2r_{ot}(\theta))}{d\theta} = 0 \quad (18)$$

and θ_0 must satisfy $\theta_0 \in (0_1, 0_2)$ for $i=1$, and $\theta_0 \in (0_2, 0_1)$ for $i=2$.

For the PTR of CAT, URT, and HSAR given in section 2, their the stationary-phase point θ_0 can be solved as follows.

(1) CAT- Parallel Beam

$$\theta_0 = \varphi + \sin^{-1}\left(\frac{\Theta}{R \cdot r_t}\right) \quad (19)$$

(2) CAT- Fan Beam

$$\theta_0 = \varphi - \sin^{-1}(x), \text{ where } x = \frac{-B \pm \sqrt{B^2 - 4AC}}{2A}, \quad (20)$$

$$A = \Theta, \quad B = -2 \frac{r_s}{\tan \gamma} \Theta + R \left(\frac{r_s}{\tan \gamma} \right)^2, \quad C = \left(\frac{r_s}{\tan \gamma} \right)^2 \Theta - R \frac{r_s}{\tan \gamma} r_t^2$$

(3) HSAR or URT

$$\theta_0 = \varphi - \cos^{-1}(x), \text{ where } x = \frac{-B \pm \sqrt{B^2 - 4AC}}{2A}, \quad (21)$$

$$A = (2 R r_s r_t)^2, \quad B = -2 r_s r_t \Theta^2, \quad C = -(2 R r_s r_t)^2 + \Theta^2 (r_s^2 + r_t^2)$$

Obviously, the frequency range of the frequency modulation signal $e^{-j2\pi r_{ot}(\theta', r, \theta)R}$ is linearly proportional to R and (linearly or nonlinearly) proportional to r . This frequency range becomes zero at $R = 0$ or $r = 0$. More detailed analysis of the frequency range of each system is given in Section 5. Therefore, the energy distribution of the 2-D spectrum of the PTR is a triangular shaped function as shown in Figure 8. The spectrum magnitude can also be obtained directly from a fast Fourier transform process as shown in Figure 9a through 9c for three typical systems. These examples are given by a point target with $r_t = r_s$. For the fan beam CAT case, the triangle is skewed due to the unsymmetric slopes of the ascending and descending line segments in the PTR shown in Figure 7b.

The total integrated energy along any line of constant R is given by

$$P(R) = \int_0^{2\pi} \left| \int e^{-j2\pi r_{st}(\theta', r, 0)R} \cdot e^{-j2\pi \theta' \Theta} d\theta' \right|^2 d\Theta \quad (22)$$

According to Parseval's theorem, this integrated energy can be rewritten as

$$P(R) = \int_0^{2\pi} |e^{-j2\pi r_{st}(\theta', r, 0)R}|^2 d\theta' = 2\pi \quad (23)$$

This indicates that the total integrated energy along any line of constant R is a constant. Therefore, if this energy is uniformly distributed within the triangle, its magnitude must be equal to $R^{-1/2}$ as shown in Figure 9d. The 1-D cuts of these spectra are plotted in Figure 10a through 10d. In general, the magnitude profiles follows that predicted by Eq. (16). The high frequency variation in Figure 10a and 10b is due to the result of the superposition of the two segments of the frequency modulation signals in Eq. (13). In CAT systems, the two segments contains the identical information, so that one segment can be ignored. In a SAR and an URT system, these two segments represents echoes reflected from the opposite sides of the target. Thus processing with both segments may be desirable.

4. WEIGHTING FUNCTION SELECTION

In this section, it will be shown that proper weighting function can be chosen to match the PSFS to those of several reported algorithms. In SAR processing, to maximize the resolution, it is common to select an inverse filter [30], in which the amplitude is the reciprocal of the 2-D spectrum. Hence, the weighting function $W_r(R, \Theta)$ is the square of the reciprocal of the 2-D spectrum. This weighting function will be denoted as $|E_{pt-r}(R, \Theta)|^{-2}$. However, it is of great interest to chose $W_r(R, \Theta)$ to be the square of the reciprocal of the 2-D spectrum shown in Figure 9d, or equivalently the absolute value of R , then Eq. (10) can be rewritten as

$$\sigma(r, \theta) = \iint E(R, \Theta) \cdot |R| \cdot \left(\iint \delta(r' - r_{ot}(\theta', r, 0)) e^{j2\pi r'R} e^{j2\pi \theta'\Theta} dr' d\theta' \right) e^{j2\pi \theta \Theta} dR d\Theta \quad (24)$$

By eliminating the delta function and replacing $E(R, \Theta)$ with the angular Fourier transform of its 1-D range spectrum $E_I(R, \theta_1)$, it can be shown that

$$\sigma(r, \theta) = \iint \left(\int E_I(R, \theta_1) e^{-j2\pi \theta_1 \Theta} d\theta_1 \right) \cdot |R| \cdot \left(\int e^{j2\pi r_{ot}(\theta', r, 0)R} e^{j2\pi \theta' \Theta} d\theta' \right) e^{j2\pi \theta \Theta} dR d\Theta \quad (25)$$

Since $\int e^{-j2\pi\theta_1\Theta} e^{j2\pi\theta'\Theta} e^{j2\pi\theta\Theta} d\Theta = \delta(\theta_1 - (\theta + \theta'))$, Eq. (25) can be further reduced to

$$\begin{aligned}\sigma(r, \theta) &= \iint E_I(R, \theta + \theta') \cdot |R| \cdot e^{j2\pi r_{ot}(\theta', r, 0)R} dR d\theta' \\ &= \iint E_I(R, \theta') \cdot |R| \cdot e^{j2\pi r_{ot}(\theta', r, \theta)R} dR d\theta'\end{aligned}\quad (26)$$

For a parallel beam CAT, $r_{ot}(\theta', r, \theta) = r \cdot \cos(\theta' - \theta)$, therefore,

$$\sigma(r, \theta) = \iint E_I(R, \theta') \cdot |R| \cdot e^{j2\pi R r \cos(\theta' - \theta)} dR d\theta' \quad (27)$$

Eq. (27) is identical to Eq. (23) in [6], which directly leads to the CBP algorithm. The PSF of the reconstructed image for a point target using the CBP algorithm can be found in Appendix A.

Let us consider the SAR and URT cases. If the weighting function $W_r(R, \Theta)$ is, however, chosen to be

$$W_r(R, \Theta) = |R| \cdot \frac{E_{pt-r}(R, \Theta) \otimes W_1(R, \Theta)}{E_{pt-r}(R, \Theta)}, \quad (28)$$

where $W_1(R, \Theta) = \int (r_s / r_{ot}(\theta', r, 0)) e^{-j2\pi \theta' \Theta} d\theta'$ and $E_{pt-r}(R, \Theta)$ is the 2-D spectrum of a point target located at $(r, 0)$. Then for a single point target located at (r_1, θ_1) , its PSF can be written as the following based on Eq. (10).

$$\sigma_{pt}(r, \theta) = \iint e^{-j2\pi r_{ot}(\theta', r_1, \theta_1)R} \cdot \left(|R| \cdot \left(\frac{r_s}{r_{ot}(\theta', r, \theta)} \right)^2 \right) e^{j2\pi r_{ot}(\theta', r, \theta)R} dR d\theta' \quad (29)$$

where σ_{pt} denotes the PSF of a point target. Since the PSF resembles a delta function, only the sidelobe near the peak are interested here. In other words, we want to obtain the value of $\sigma_{pt}(r, \theta)$ at (r, θ) where $r - r_1$ and $\theta - \theta_1$ are very small. By using the approximation

$$r_{ot}(\theta', r, \theta) - r_{ot}(\theta', r_1, \theta_1) \cong r_s (r_1 \sin(\alpha' + \Delta\theta) - r \sin(\alpha')) / r_{ot}(\theta', r, \theta), \quad (30)$$

Eq. (29) can be expressed as

$$\sigma_{pt}(r, \theta) = \iint (|R| \cdot \left(\frac{r_s}{r_{ot}(\theta', r, \theta)} \right)^2) e^{j2\pi \frac{(r_s r_1 \sin(\alpha' + \Delta\theta) - r_s r \sin(\alpha'))}{r_{ot}(\theta', r, \theta)} R} dR d\theta' \quad (31)$$

where $\Delta\theta = \theta - \theta_1$. By changing variable from R to $R' = R \cdot \left(\frac{r_s}{r_{ot}(\theta', r, \theta)} \right)$, Eq. (31) is given by

$$\sigma_{pt}(r, \theta) = \iint R' e^{j2\pi(r_1 \sin(\alpha' + \Delta\theta) - r \sin(\alpha')) R'} dR' d\theta' \quad (32)$$

Equation (32) is identical to (A2). Therefore, the resulting ISF also follows that of the Fraunhofer diffraction of a circular aperture. This is also true for the exact inversion algorithm [7] (see Appendix B).

Similarly, for a fan beam CAT system, the weighting function with the following form would yield an PSF having the ideal $J_1(\sim;)/(2r\delta r)$ form.

$$W_r(R, \Theta) = |R| \cdot \frac{E_{pt-r}(R, \Theta) \otimes W_2(R, \Theta)}{E_{pt-r}(R, \Theta)}, \quad (33)$$

$$\text{where } W_2(R, \Theta) = \int \left(\frac{r_s / \tan \gamma}{r_s / \tan \gamma - r_t(\theta)} \right)^2 e^{-j2\pi \theta' \Theta} d\theta'.$$

The weighting functions suggested in this section allow the image reconstructed with an ideal PSF form. If further shaping to the PSF is required to reduce the sidelobes, one can simply add an additional weighting, expressed the function of R , to the first one. Detailed analysis on the performance of various type of weighting functions can be found in [33].

5. SAMPLING SPACING AND RESOLUTION

According to the Nyquist theorem, the range sampling spacing must follow the range bandwidth, which is determined by the pulses transmitted by the radar or the ultrasonic transducer or determined by the x-ray beam width for the CAT systems. The azimuth sampling spacing, or the azimuth sampling angle, can be determined by two

reasonings. The first reasoning can be illustrated by Figure 11 for a parallel beam CAT system. The two lines represent the spectra of two projections. At each end of the spectra, the spacing between two lines must be no less than the resolution width of the spectra. Since the resolution of the spectra is given by the ratio of the range bandwidth F to the number of samples received N_s , the azimuth angle spacing is given by $2 / N_s$. For one complete circle, the total number of azimuth samples is therefore equal to $\pi \cdot N_s$.

The second reasoning for the azimuth sampling angle is a more general one. It is based on the maximum azimuth bandwidth of the PTR. The azimuth angular frequency profile is given by

$$\Theta(\theta) = \frac{d R \cdot r_{ot}(\theta)}{d\theta}. \quad (34)$$

For a parallel beam CAT, it follows that $\Theta(0) = R \cdot r_t \cdot \sin \theta$. The maximum and minimum angular frequencies are therefore $\pm R \cdot r_t$. Since $|R| \leq 1 / (2\delta r)$ and $r_t \leq r_s$, the maximum azimuth angular frequency bandwidth is $2r_s / (2\delta r)$. This is further reduced to $N_s / 2$ by letting $N_s = 2r_s / \delta r$. Now, we reach the same conclusion that the minimum azimuth angle spacing must be no less than $2 / N_s$. For a fan beam CAT, it can be shown that maximum azimuth angular frequency bandwidth is $(r_s / \delta r) \cdot (\sin^2 \gamma / \cos(2\gamma))$. Since the factor $(\sin^2 \gamma / \cos(2\gamma))$ is less than one, the azimuth angle spacing for a fan beam CAT must be finer than $2 / N_s$.

For a URT system, The maximum azimuth angular frequency bandwidth is r_s / δ . Similarly, for this system the minimum azimuth angle spacing must be no less than $2 / N_s$. For a HSAR system, the maximum azimuth angular frequency bandwidth is $(r_s / \delta r) \cdot (2r_s^2 h \sqrt{h^2 + 4r_s^2}) \cdot r_s^{-1}$. The factor $(2r_s^2 + h^2 - \sqrt{h^2 + 4r_s^2}) \cdot r_s^{-1}$ is greater than one, therefore, the azimuth angle spacing for a HSAR system must be greater than $2 / N_s$.

The azimuth spatial resolution is determined by the product of the distance between the target and the center of circle and the reciprocal of the azimuth angular bandwidth. The azimuth angular bandwidth as a function of the target to center distance are summarized below:

(1) Parallel Beam CAT and URT

$$B_a(r_t) = r_t / \delta r \quad (35)$$

(2) Fan Beam CAT

$$B_a(r_t) = \beta_1(r_t) \cdot r_t / \delta r \quad (36)$$

where $\beta_1(r_t) = (r_s / \tan \gamma)^2 / ((r_s / \tan \gamma)^2 - r_t^2)$.

(3) Holographic Synthetic Aperture Radar

$$B_a(r_t) = \beta_2(r_t) \cdot r_t / \delta r \quad (37)$$

$$\text{where } \beta_2(r_t) = \frac{\sqrt{2r_s^2 r_t^2 + \frac{1}{2}(h^2 + r_s^2 + r_t^2)^2 \left(\frac{\sqrt{(h^2 + r_s^2 + r_t^2)^2 - 4r_s^2 r_t^2}}{(h^2 + r_s^2 + r_t^2)} - 1 \right)}}{r_t \cdot \sqrt{(h^2 + r_s^2 + r_t^2)^2 - 4r_s^2 r_t^2}}$$

It is obvious that for the parallel beam CAT and the URT systems, the azimuth spatial resolution is equal to a constant of δr . For the fan beam CAT system and the HSAR system, the azimuth spatial resolution is equal to a constant of $\delta r / \beta_1(r_t)$ and $\delta r / \beta_2(r_t)$, respectively. The azimuth spatial resolution of these four systems are plotted in Figure 12. After all, the actual resolution of the final image is also affected by the weighting functions applied.

6. SIMULATION RESULTS

A simulation was performed to test the proposed algorithm and to verify the analysis on the PSF resolution. The received data is the simulated echo of ten point targets distributed along a spiral curve for various angles and target-to-center distances. The point targets are reconstructed using the proposed algorithm with several different weighting functions. Finally, these images are oversampled and resampled to the rectangular coordinate to better reveal their PSF shapes.

Shown in Figure 13a and 13b are the PSFs for the parallel beam CAT system with a weighting of $|R|$ and an inverse filter weighting $|E_{pt-r}(R, @)^{-1/2}$, respectively. Each image only has 64 resolution cells along the diameter of the image. The grey levels of these images

are adjusted to let the sidelobes shown more clearly. One can see the one with the inverse filter has significantly worse sidelobes. Figure 13c shows the PSFS with a weighting of $|R| \cdot K_\alpha(R, \alpha)$ and $\alpha = 0.8$. Where $K_\alpha(R, \alpha)$ is a Kaiser weighting and α is the weighting coefficient. These PSFs have a lightly worse resolution but much better sidelobe performance. The resolution of the PSF in Figure 13a is directly measured from the oversampled data. Its 3-dB resolution is given by $1.029\delta r$ as that predicted from the Fraunhofer diffraction of a circular aperture. Figure 12d shows the PSFS obtained directly from the form of $J_1(\frac{r}{2\delta r}) / (2r\delta r)$. There is very little difference between Figure 13a and 13d. The simulated PSFS for the fan beam CAT, HSAR, and URT systems are also obtained. Their PSFS with different weighting functions are very similar to that of Figure 13a through 13c.

In HSAR and URT systems, a transmitted pulse with a center frequency several times greater than the pulse bandwidth (see Figure 6b) may be considered. A simulation was carried out with a pulse bandwidth only .133 times of the carrier frequency. Its PSF is shown in Figure 14. This PSF exactly follows that of the Fraunhofer diffraction of a ring aperture. The 3-dB resolutions of this case is still close to $1.029 \delta r$. But, it has a much worse integrated sidelobe ratio.

7. IMPLEMENTATION APPROACH

In general, the image reconstruction process based on Eq. (10) consisted of five steps: (1) transforming the data echo into its 2-D spectrum, (2) generating the reference function, (3) spectra multiply and summation in range, (4) Inverse Fourier transformation in azimuth, and (5) convert image pixels from a polar coordinate into a Cartesian coordinate. For the HSAR case a slant to ground range conversion maybe inserted between step (4) and (5). Obviously, the fast Fourier transform (FFT) is the most efficient for steps (1) and (4). In multiplying the reference function to the data spectrum a large number of multiplications can be saved due to the characteristic cs of the reference functions. First, there is about 75% of the total samples in the reference functions associated the value of zero. This is because the number of zeroes in each reference function set changes linearly (or nearly linearly) from 50% to approximately 100% for their corresponding r value varying from r_s to zero. In addition, the spectrum in the half plane with negative R values is the complex conjugate of the other half of the plane. This represents an additional 50% reduction of the multiplications. Overall, the number of multiplications required is only 12.5% of the total number of samples in the reference functions.

Reference functions may be realized either based on the analytical solution given in Eq. (15) or by taking a 2-D FFT on the point target response. For systems with relatively small number of data samples such as CAT and URT, the reference functions may be generated by the later approach for higher accuracy. To avoid a loss in the processing efficiency, the reference functions may be generated before data processing and stored in computer memory permanently. For a fan beam CAT with 320 X 320 image pixels, the amount of memory required for all 160 sets of reference functions is about 21 MB (mega bytes), which is well within the capacity of the most present day baseline computers. For a parallel beam CAT, the memory size required is even less. This is because that among all 160 sets of spectra, each corresponding to a unique target to center distance, there is a redundancy due to that $R \cdot \text{rot}(e)$ in Eq. (15) and (16) has the property of

$$R \cdot \text{rot}(\theta) = R \cdot r_t \cos \theta = c_1 R \cdot \frac{r_t}{c_1} \cos \theta \quad (38)$$

Another words, the spectra $E_{pt-r_t}(R, \theta)$ used for focusing target at r_t is equal to the spectra $E_{pt-r_t/c_1}(c_1 \cdot R, \theta)$ used for focusing target at r_t/c_1 .

To be noted is that the PTR modeling for a fan beam CAT is simplified in this paper. In implementing a fan beam CAT data processor, one must take into account the effect of varying range resolution, due to the changing distance between the x-ray source and the target, in the PTR obtained from all azimuth angles.

8. DISCUSSION

Although the operations (multiplications and additions) required by using this algorithm is $O(N^3)$, the actual number of operations is much better than the CBP algorithm for the reasons given in section 7. For a CAT system with pre-generated reference functions, the number of operations required to generate an image with 320 X 320 pixels is estimated to be within 50 million. This is approximately one order of magnitude lower than the CBP algorithm. Furthermore, for systems with 320 X 320 image pixels the number of operations is also very close to that of the direct inverse FFT algorithm.

Aside from its superior computation efficiency, the proposed algorithm also produces images with better quality. In the proposed algorithm, the interpolation for

converting image pixels into a Cartesian grid is performed on real-valued image pixels with its full resolution. The interpolation error correlates with the magnitude of the local image pixels. Another words, image pixels with higher intensity are associated with grater interpolation error and image pixels with lower intensity are associated with lower interpolation error. In the direct Fourier algorithm [13], the interpolation for the converting the spectrum coordinate is performed on complex-valued spectra samples. After inverse FFT, the effect of interpolation error is uniformly distributed in the final image. Therefore, image pixels with lower intensity may be associated with higher error. This explains why the degradation of interpolation in the proposed algorithm is less significant than the spectrum interpolation involved in the direct inverse FFT algorithm. In the CBP algorithm, the convolution process can also be viewed as a large number of interpolations. The interpolator is its kernel function [6]. To improve image quality by using a longer kernel would increase the total number of operation by $O(N^3)$. However, in the proposed algorithm, to improve image quality by using a longer interpolator would increase the total number of operation by $O(N^2)$. Therefore, the proposed algorithm is also more cost effective in the trade-off between the computation load and image quality.

In any imaging systems, there exists certain amount of the system thermal noise. This noise is caused by the quantization error, the environment noise (for radar and ultrasonic), and sensor noise. Since the input data samples are in a polar grid, the number of samples near the center is more dense than that near the imaging circle and exceeds that required by the Nyquist rate. Therefore, one may use a low pass filter in the azimuth dimension with a bandwidth tuned for each radius to reduce the thermal noise. Another reason for performing low pass filtering is to remove the artifact of azimuth aliasing [13]. In both the proposed algorithm and the CBP algorithm, the low pass filtering is effectively accomplished without extra computation. However, for the direct inverse FFT algorithm, low pass filtering does impose extra computation load to the overall processing.

Although this paper is limited to the systems of circular symmetric observations, the PTR formulation, 2-D spectra analysis, and the image reconstruction algorithm may be applied back to the straight line path systems such as a wide beam, wide band airborne SAR. Similarly, it may also be applied to narrow beam and narrow band spotlight SAR. In addition, its application may be extended into the 3-D imaging area. An example of this is an URT system shown in Figure 15. The imaging observation points is uniformly distributed on the curved surface of a cylinder surrounding the object.

9. SUMMARY

This paper uses the point target response to formulate a general image reconstruction solution to several imaging systems including HSAR, CAT, and URT systems. The proposed algorithm is also applicable to many other systems mentioned in this paper. The quality of images generated by this algorithm is superior to other previously reported algorithms. By incorporating proper weighting functions, the resulting PSFs can be made exactly following that predicted by the Fraunhofer diffraction. In addition, further shaping for the PSF may be achieved by applying extra weighings. This algorithm can be implemented in several different ways. When applied to the CAT system, its throughput rate is an order of magnitude higher than the commonly used convolution backprojection algorithm.

APPENDIX A POINT SPREAD FUNCTION OF CAT WITH CBP ALGORITHM

According to [6], the parallel beam CAT image reconstructed by the CBP algorithm can be expressed by

$$\sigma(r, \theta) = \iint E_I(R, \theta') |R| \cdot e^{j2\pi \cdot R \cdot r \cos(\theta' - \theta)} dR d\theta', \quad (A1)$$

where $E_I(R, \theta')$ is the Fourier transform of the projection at angle θ' . In order to derive the PSF, we substitute $E_I(R, \theta')$ with that resulted from a point target located at (r_1, θ_1) .

$$\sigma_{pt}(r, \theta) = \iint e^{j2\pi \cdot R \cdot r_1 \cos(\theta' - \theta_1)} |R| \cdot e^{j2\pi \cdot R \cdot r \cos(\theta' - \theta)} dR d\theta' \quad (A2)$$

Equation (A2) can also be expressed as

$$\sigma_{pt}(r, \theta) = \iint (A(R, \theta') \cdot B(R, \theta')) |R| \cdot e^{j2\pi \cdot R \cdot r \cos(\theta' - \theta)} dR d\theta' \quad (A3)$$

where $A(R, \theta') = e^{j2\pi \cdot R \cdot r_1 \cos(\theta' - \theta_1)}$, , for $-\infty \leq R \cos \theta' \leq \infty$,

$$\text{and } -\infty \leq R \sin \theta' \leq \infty,$$

$$\begin{aligned} \text{and } B(R, \theta') &= 1, \text{ for } 0 \leq R \leq \frac{1}{2\delta r} \text{ and } 0 \leq \theta' \leq 2\pi. \\ &= 0, \text{ otherwise} \end{aligned}$$

Since the Fourier pair of the product of two functions is equal to the convolution of the Fourier pairs of each individual one, we have

$$\begin{aligned} \sigma_{\text{pt}}(r, \theta) &= \iint A(R, \theta') \cdot |R| \cdot e^{j2\pi \cdot R \cdot r \cos(\theta' - \theta)} dR d\theta' \\ &\otimes \iint B(R, \theta') \cdot |R| \cdot e^{j2\pi \cdot R \cdot r \cos(\theta' - \theta)} dR d\theta' \end{aligned} \quad (\text{A4})$$

The result of equation (A4) is simply

$$\sigma_{\text{pt}}(r, \theta) = \delta(r \cos \theta - r_1 \cos \theta_1, r \sin \theta - r_1 \sin \theta_1) \otimes \left(J_1\left(\frac{r}{2\delta r}\right) / (2r\delta r) \right) \quad (\text{A5})$$

This is a PSF of a point target centered at (r_1, θ_1) with the shape of $J_1\left(\frac{r}{2\delta r}\right) / (2r\delta r)$, which is the Fraunhofer diffraction pattern of a circular aperture [34].

APPENDIX B POINT SPREAD FUNCTION OF NORTON'S SOLUTION

According to [7], the image can be reconstructed by the following equation

$$\sigma(r, \theta) = \sum_{n=-\infty}^{\infty} H_n \left\{ \frac{1}{J_n(Rz)} H_0 \left\{ \frac{g_n \sqrt{P}}{2\pi\rho} \right\}^{jn\theta} \right\} \quad (\text{B1})$$

where H_0 and H_n are the Hankel transform operator of the 0-th and n-th order, respectively, $J_n(x)$ is the Bessel function of the n-th order, and

$$g_n(\rho) = \int g(\rho, \theta) e^{-jn\theta} d\theta. \quad (\text{B2})$$

where $g(\rho, \theta)$ is the data received by the sensor. To obtain the PSF of a point target, one must replace $g(\rho, \theta)$ with a point target response. Assuming that the point target is located at (r_1, θ_1) , then according to Eq. (B2), its harmonic expansion can be expressed as

$$g_n(\rho) = e^{-n\theta_1} \int_0^{2\pi} d\phi \delta[(r_1^2 + R^2 - 2r_1 R \cos \phi)^{1/2} - \rho] e^{-n\phi} \quad (\text{B3})$$

The R in (B3) is the r_s in this paper. using Eq. (9) in [7], Eq. (B3) can be reduced to

$$g_n(\rho) = e^{-n\theta_1} 2\pi\rho \int_0^\infty dz \cdot z J_0(\rho z) J_n(zR) J_n(zr_1) \quad (\text{B4})$$

By inserting Eq. (B4) into Eq. (B1) and changing the notation of $\sigma(r, \theta)$ to $\sigma_{\text{pt}}(r, \theta)$, we have

$$\sigma_{\text{pt}}(r, \theta) = e^{-n\theta_1} \sum_{n=-\infty}^{\infty} \int_0^\infty dz \cdot z J_n(zr) J_n(zr_1) e^{jn\theta} \quad (\text{B5})$$

By inserting the Bessel functions into Eq. (B5), it is then given by

$$\sigma_{\text{pt}}(r, \theta) = \frac{1}{(2\pi)^2} \sum_{n=-\infty}^{\infty} e^{-n\theta_1} \int_0^\infty dz \cdot z \left(\int_{-\pi}^{\pi} e^{j(n\alpha - zr \sin \alpha)} d\alpha \right) \cdot \left(\int_{-\pi}^{\pi} e^{j(n\alpha' - zr_1 \sin \alpha')} d\alpha' \right) e^{jn\theta} \quad (\text{B6})$$

Using the identity of $\sum_{n=-\infty}^{\infty} e^{-jn(\theta_1 - \alpha - \alpha' - \theta)} = \delta(\theta_1 - \alpha - \alpha' - \theta)$ and changing the

variable z to $2\pi \cdot R$, (B6) can be further reduced to

$$\sigma_{\text{pt}}(r, \theta) = \int_0^\infty R \cdot e^{-dR} dR \cdot \left(\int_{-\pi}^{\pi} e^{j2\pi R r_1 \sin(\alpha + (\theta - \theta_1))} d\alpha \right) \quad (\text{B7})$$

The sine function can be replaced by a cosine function since the integration is over a complete cycle. Therefore, Eq. (B7) is identical to Eq. (A2) and its PSF can be expressed in Eq. (A5).

Reference:

- [1] Shepp, L. A. and Logan, B. F., "The Fourier reconstruction of a head section", IEEE Transactions on Nuclear Sciences, vol. NS-21, pp. 21-42, 1974.
- [2] Norton, S. J., "Reconstruction of a two-dimensional reflecting medium over a circular domain: exact solution", J. Acoust. Soc. Am., 67(4), 1980.
- [3] Glazner, J. K., DiRosa, D. A., "A comparison between holographic SAR (HSAR) and conventional narrow angle SAR", presented at the European Association of Remote Sensing Laboratories' Workshop on Microwave Imaging and Related Techniques, Albach, Australia, December 2-4, 1991.
- [4] Schindel, R. F., Experimental Diverse Microwave Holograph, Ph.D. Dissertation, UT-Arlington, Arlington, Texas, December, 1989.
- [5] Wehner D. R., 1987, High Resolution Radar (Boston: Artech House).
- [6] Scudder, H. J., "Introduction to computer aided tomography", Proceedings of the IEEE, vol. 66, No. 6, June 1978.
- [7] Oppelt, A., and Grandke, T., "Magnetic Resonance Imaging", Superconductor Science and Technology, vol. 6 (6), PP: 3810395, 1993.
- [8] Cherry, S. R., "Recent advances in instrumentation for positron emission tomography", Nuclear Instruments and Methods in Physics, vol. 348 (2-3), pp. 577-582, 1994.
- [9] Macovski, A., 1983, Medical Imaging Systems (Prentice-Hall Inc.)
- [10] Radon, J., "On the determination of functions from their Integrals along certain manifolds", Ber. Seachs. Akad. Wiss. Leipzig, Math. Physics K1., vol. 69, p. 262-277, 1917.
- [11] Gordan, R., Bender, R., and Herman, G. T., "Algebraic reconstruction techniques (ART) for three dimensional electron microscopy and x-ray photography", J. Theor. Biol., vol. 29, pp. 471-481, 1970.
- [12] Mercereau, R. M. and Oppenheim, A. V., "Digital reconstruction of multidimensional signals from their projections", Proc. IEEE, vol. 62, pp. 1319-1338, 1974.
- [13] Stark, H., Woods, J. W., Paul, I., and Hingorani, R. "Direct Fourier reconstruction in computer tomography", IEEE Transactions on Acoustics, Speech, and Signal Processing, vol. ASSP-29, No. 2, pp. 237-245, April, 1981.
- [14] Martinson, L., "A programmable digital processor for airborne radar", IEEE 1975 International Radar Conference, pp. 186-191, Apr., 1975.

- [15] Walker, J. L., "Range-Doppler Imaging of Rotating Objects", IEEE Trans. on Aerospace and Electronic Systems, Vol. AES-16, No. 1, January, 1980.
- [16] Wu, C., Liu, K. Y., and Jin, M. Y., "Modeling and correlation algorithm for spaceborne SAR signals", IEEE Trans. on Aerospace and Electronic Systems, vol. AES-18, no. 5, Sept., 1982.
- [17] Ausherman, D. A., et. al., "Developments in radar imaging", IEEE Trans. on Aerospace and Electronic Systems, Vol. AES-20, No. 4, July, 1984.
- [18] Mensa, D., Heidbreder, G., and Wade, G., "Aperture synthesis by object rotation in coherent imaging", IEEE Trans. on Nuclear Science, Vol. NS-27, No. 2, April 1980.
- [19] Munson, D. C., O'Brien J. D., and Jenkins, W. K., "A Tomographic formulation of spotlight-mode synthetic aperture radar", Proceedings of the IEEE, Vol. 71, No. 8, August, 1983.
- [20] Desai, M. D. and Jenkins, W. K., "Convolution backprojection image reconstruction for spotlight mode synthetic aperture radar", IEEE Trans. on image Processing, Vol. 1, No. 4, October 1992.
- [21] Munson, D. C., Sanz, J. L., Jenkins, W. K., Kakazu, G., and Mather, B., "A comparison of algorithms for polar-to-Cartesian interpolation in spotlight mode SAR", Proc.Int.Conf. on Acoustic Speech and Signal Processing, Tampa, FL., Mar., 1985.
- [22] Mensa, D. L., Halevy, S., and Wade, G., "Coherent Doppler tomography for microwave imaging", Proceedings of the IEEE, vol. 71, No. 2, February, 1983.
- [23] Mensa, D. L., 1991, High Resolution Radar Cross-Section Imaging Ch. 4 (Boston: Artech House).
- [24] Gustavsson, A., Frolind, P. O., Hellesten, H., Jossen, T., Larsson, B., and Stenstrom, G., "The airborne VHF SAR system CARABAS", Proc.IGARSS'93, in Tokyo, 18-21, August, pp. 558-562, 1993.
- [25] Vickers, R., "Ultra-wideband radar - potential and limitations", IEEE MIT-S Digest, 1991.
- [26] Greenleaf, J. L. and Bahn, R. C., "Clinical Imaging with transmissive ultrasonic computerized tomography", IEEE Trans. Biomed. Eng., vol. BME-28, pp. 177-185, 1981.
- [27] Norton, S. J. and Linzer, M., "Ultrasonic reflectivity tomography: reconstruction with circular transducer arrays", Ultrason. Imaging, vol. 1, pp. 154-184, 1979.

- [28] Kaveh, M., and Soumekh, M., "Computer-assisted diffraction tomography", Chapter 10 of Image Recovery Theory and Application, edited by Stark, H., Academic Press, 1987.
- [29] Cafforio, C., Prati, C., and Rocca F., "SAR data focusing using seismic migration techniques", IEEE Trans. on Aerospace and Electronic Systems, vol. 27, no. 2, pp. 194-207, March, 1991.
- [30] Bamler, R., "A comparison of range-Doppler and wave-number domain SAR focusing algorithms", IEEE Trans. on Geoscience and Remote Sensing, vol. 30 (4), pp. 607-713, 1992.
- [31] Robbins, G., M. and Huang, T. S., "Inverse Filtering for Linear Shift-Variant Imaging Systems", Proc. IEEE, 60, no. 7, pp. 862-872, July, 1972.
- [32] Born, M. and Wolf, E., Principles of Optics, Pergamon Press, New York, 1959, Appendix III.
- [33] Harris, H. J., "On the use of windows for harmonic analysis with the discrete Fourier transform", Proceedings of IEEE, vol. 66, no. 1, p. 51-83, January, 1978.
- [34] Papoulis, A., Systems and Transforms with Applications in Optics, 1968 McGraw-Hill, New York, 1968.

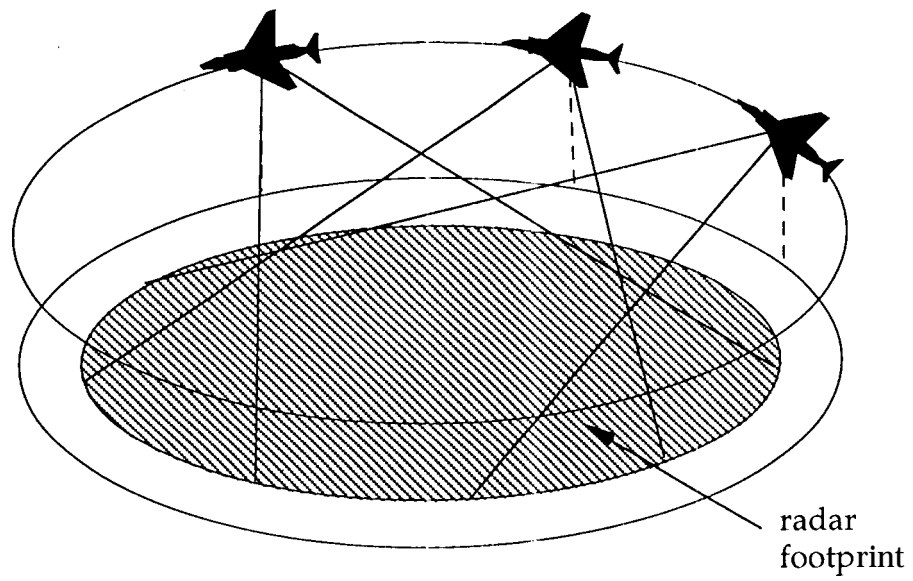


Figure 1a. Holographic SAR in circular path

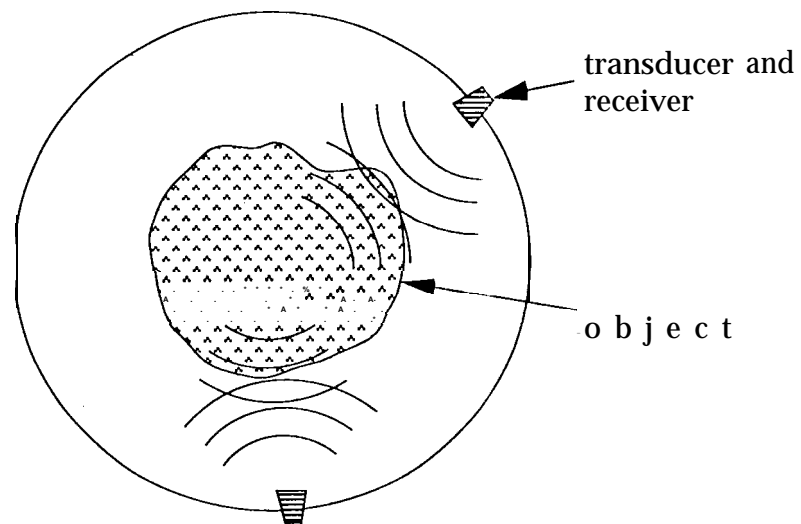


Figure 1b. Ultrasonic Reflective Tomography

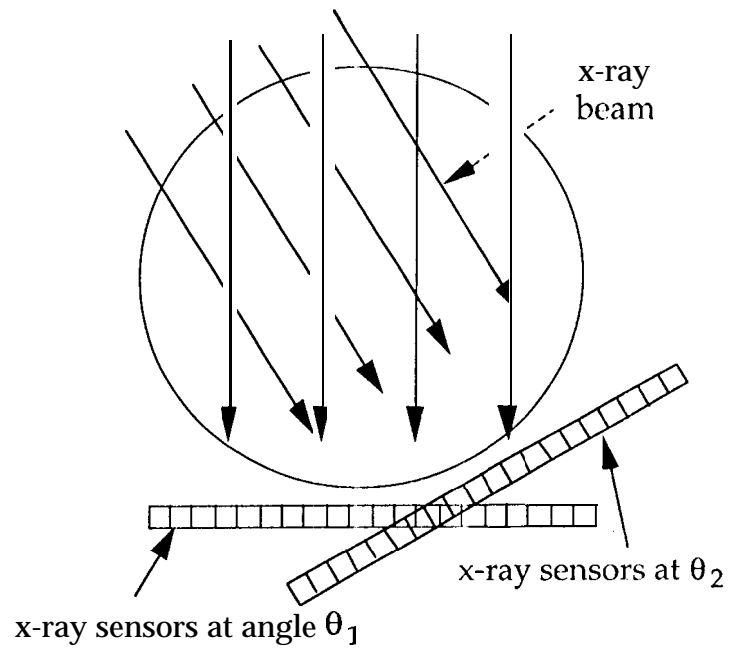


Figure 2a. Parallel Beam X-ray CAT

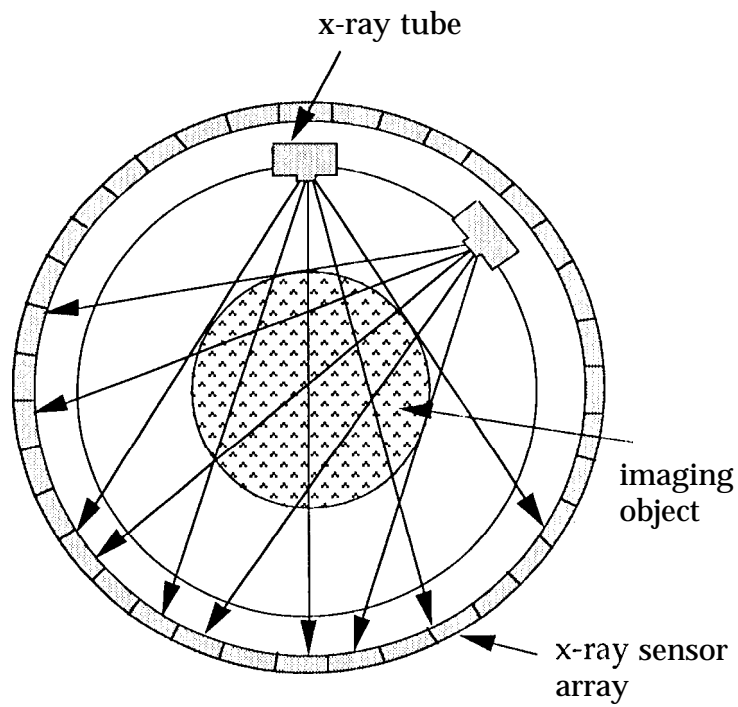


Figure 2b. Fan Beam X-ray CAT

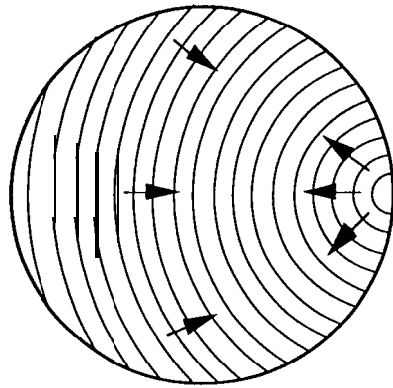


Figure 3a. Line integral along concentric circles of an ultrasonic Tomography System

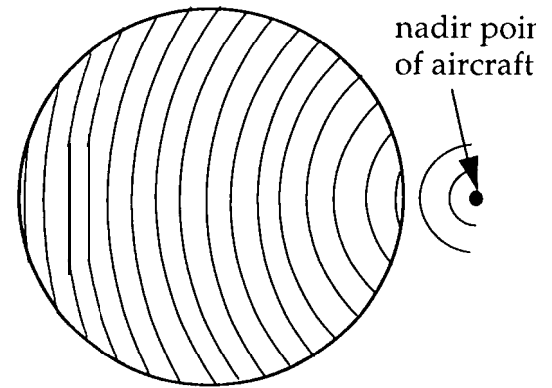


Figure 3b. Line integral along concentric circles of a holographic SAR

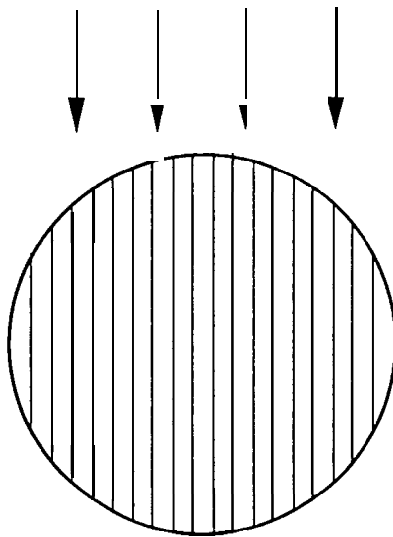


Figure 3c. Line integral along parallel lines of an X-ray computer aided tomography

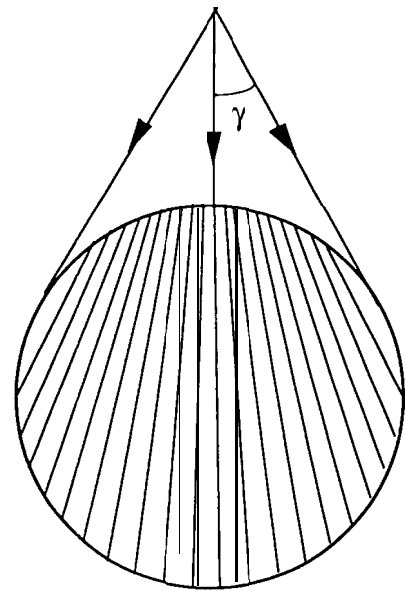


Figure 3d. Line integral along radial lines of a fan beam X-ray CAT

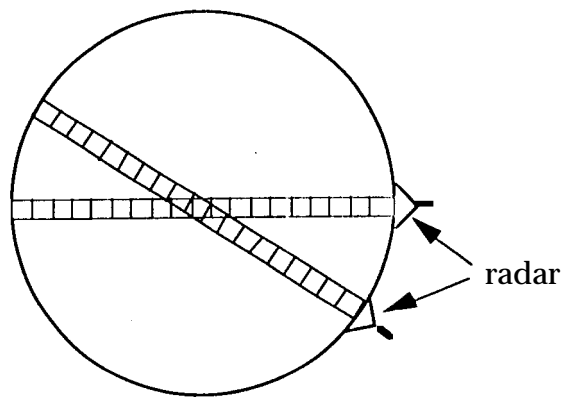


Figure 4. The resolution cells of a pencil beam radar around an imaging circle

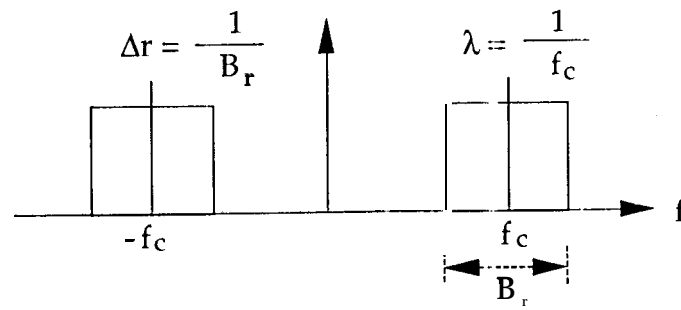


Figure 6a. The Spectrum of a Band-limited Impulse with a large carrier frequency

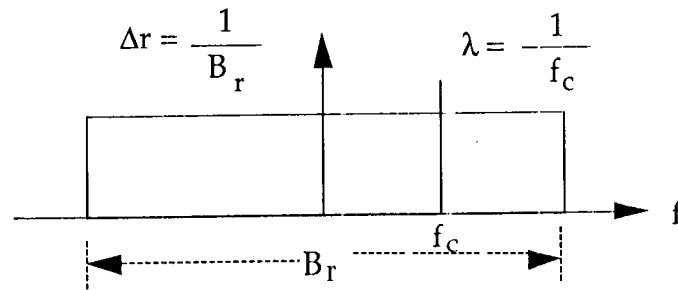


Figure 6b. The Spectrum of a Band-limited Impulse

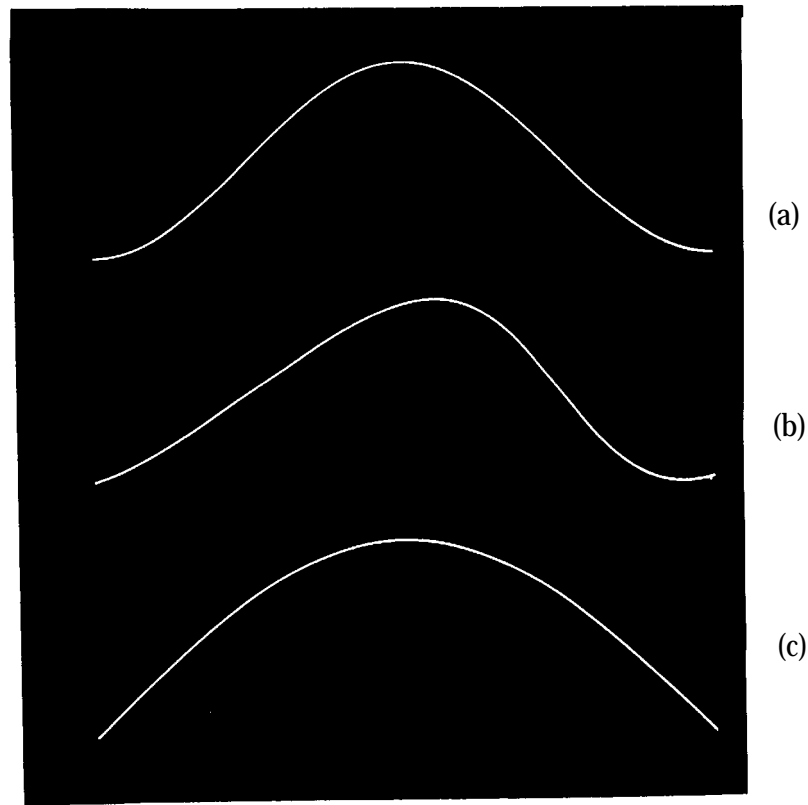


Figure 7 Point target response of (a) CAT parallel beam, (b) CAT fan beam, and (c) HSAR or URT

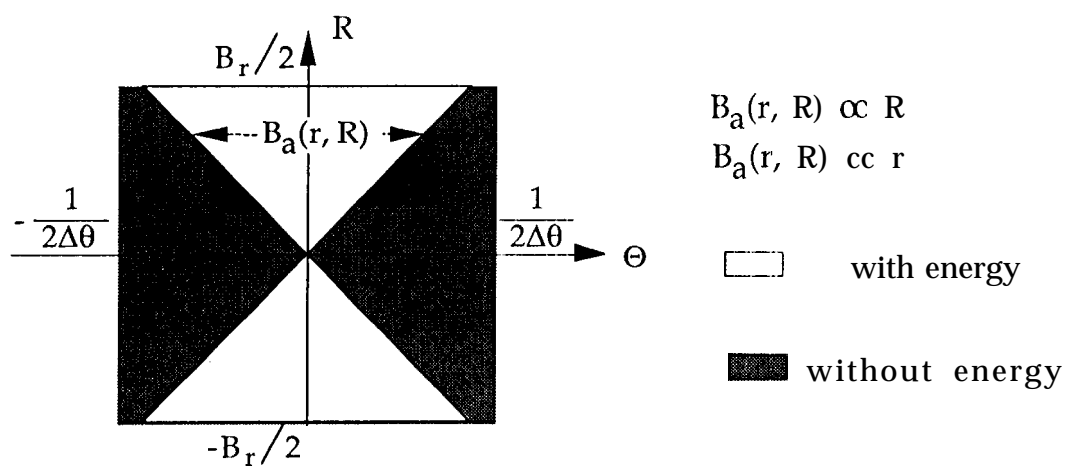


Figure 8. Energy Distribution of the Spectrum of a Point Spread Function

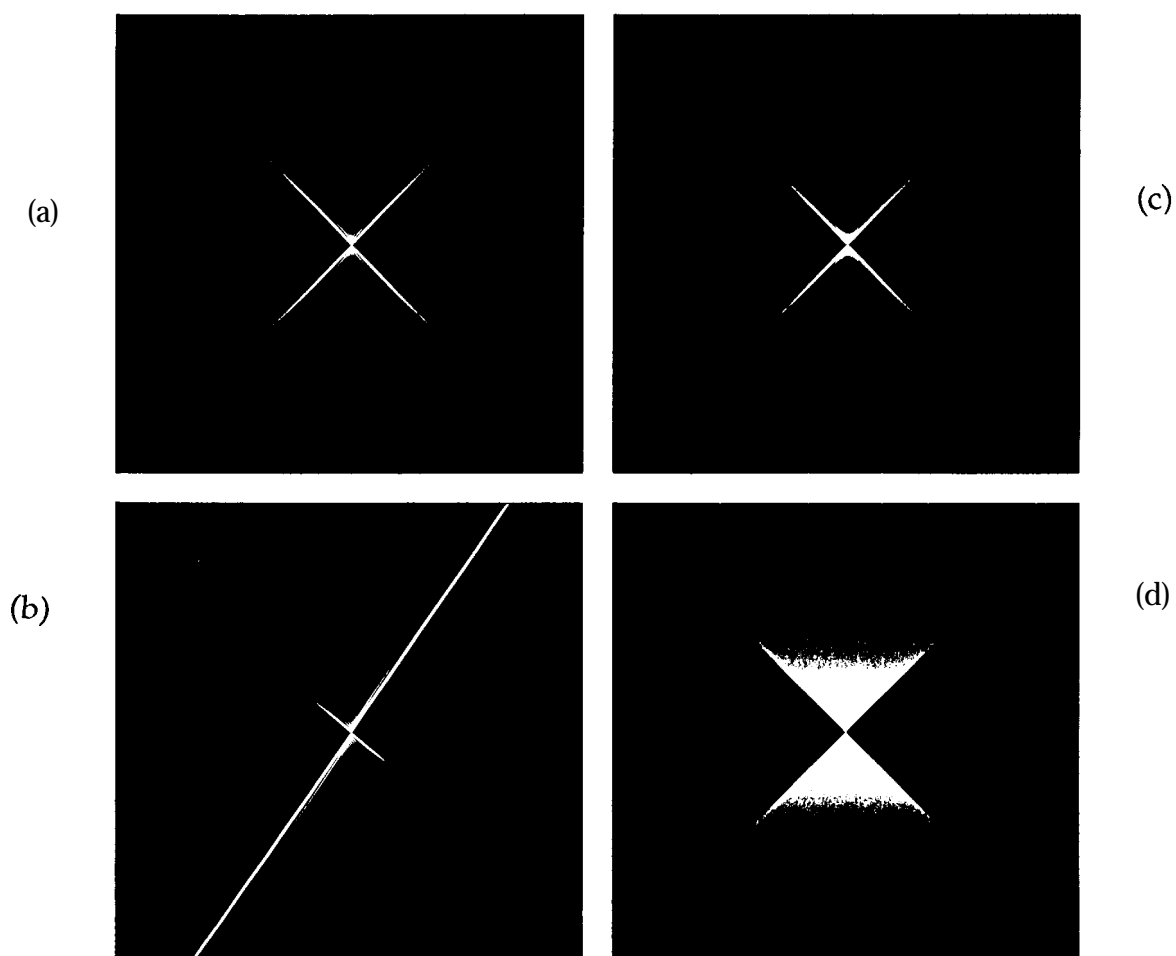
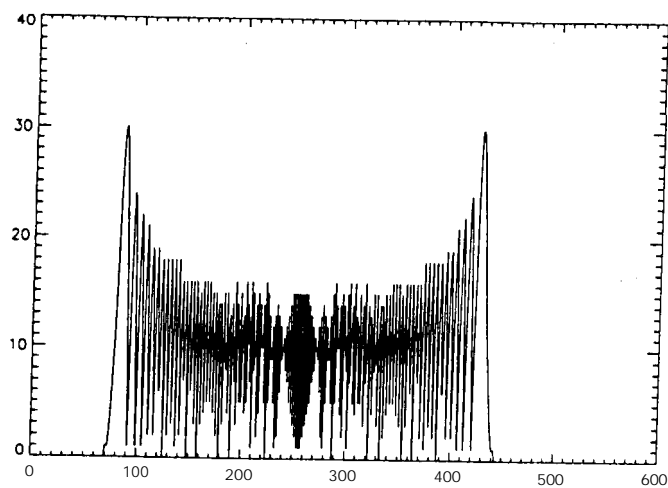
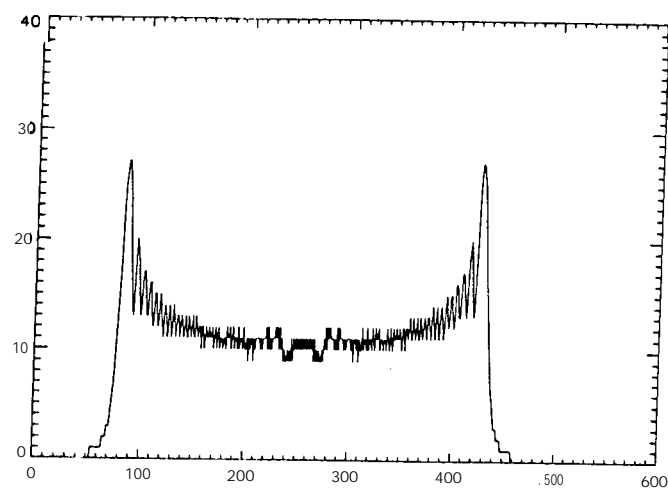


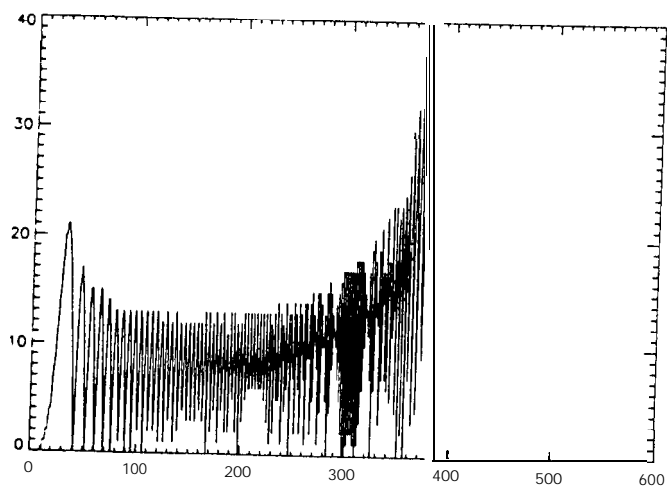
Figure 9 Magnitude of the 2-D spectrum of the PTR of (a) CAT parallel beam, (b) CAT fan beam, (c) HSAR or URT, and (d) $1/\sqrt{|R|}$



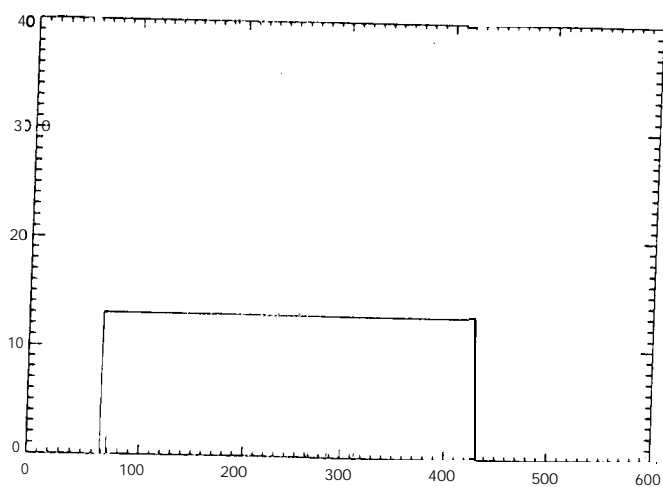
(a)



(c)



(b)



(d)

Figure 10 1-D Cut of the 2-D spectrum of the PTR
of (a) CAT parallel beam, (b) CAT fan beam,
(c) HSAR or URT, and (d) $1/\sqrt{|R|}$

$$\Delta\theta = \frac{\Delta f}{F/2} = \frac{2}{N_s}$$

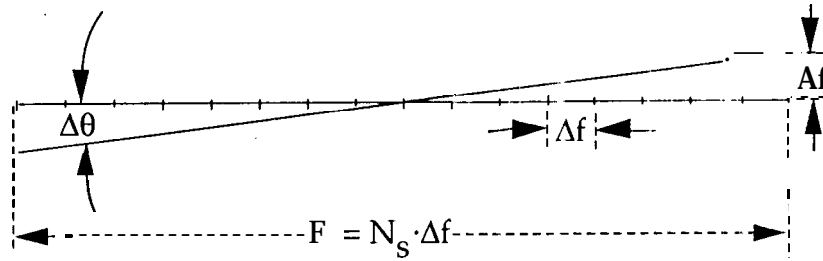


Figure 11. Azimuth sampling angle of a CAT system

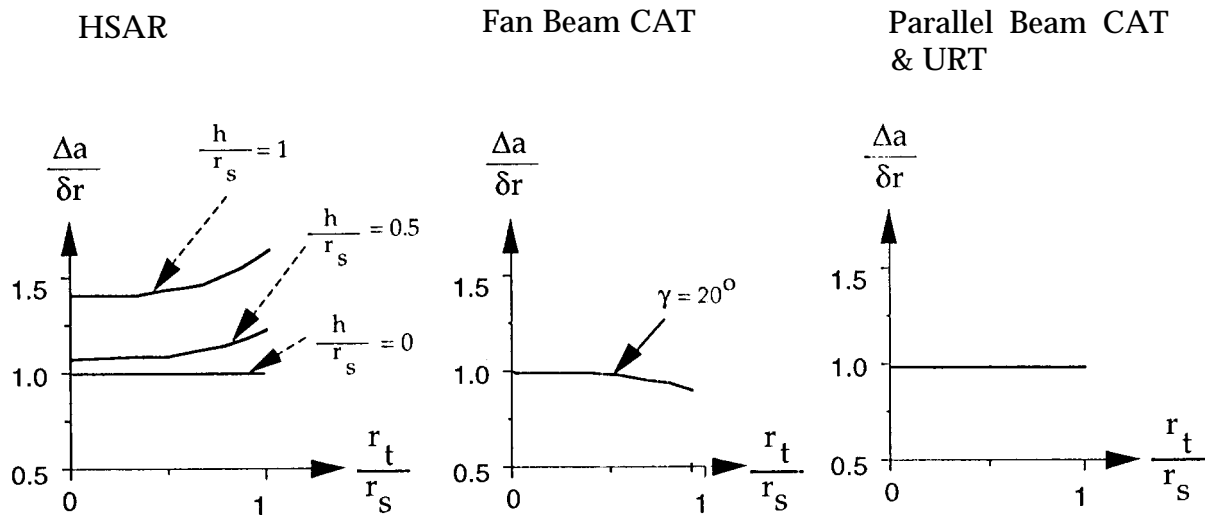


Figure 12 Azimuth spatial resolution as a function of the target position

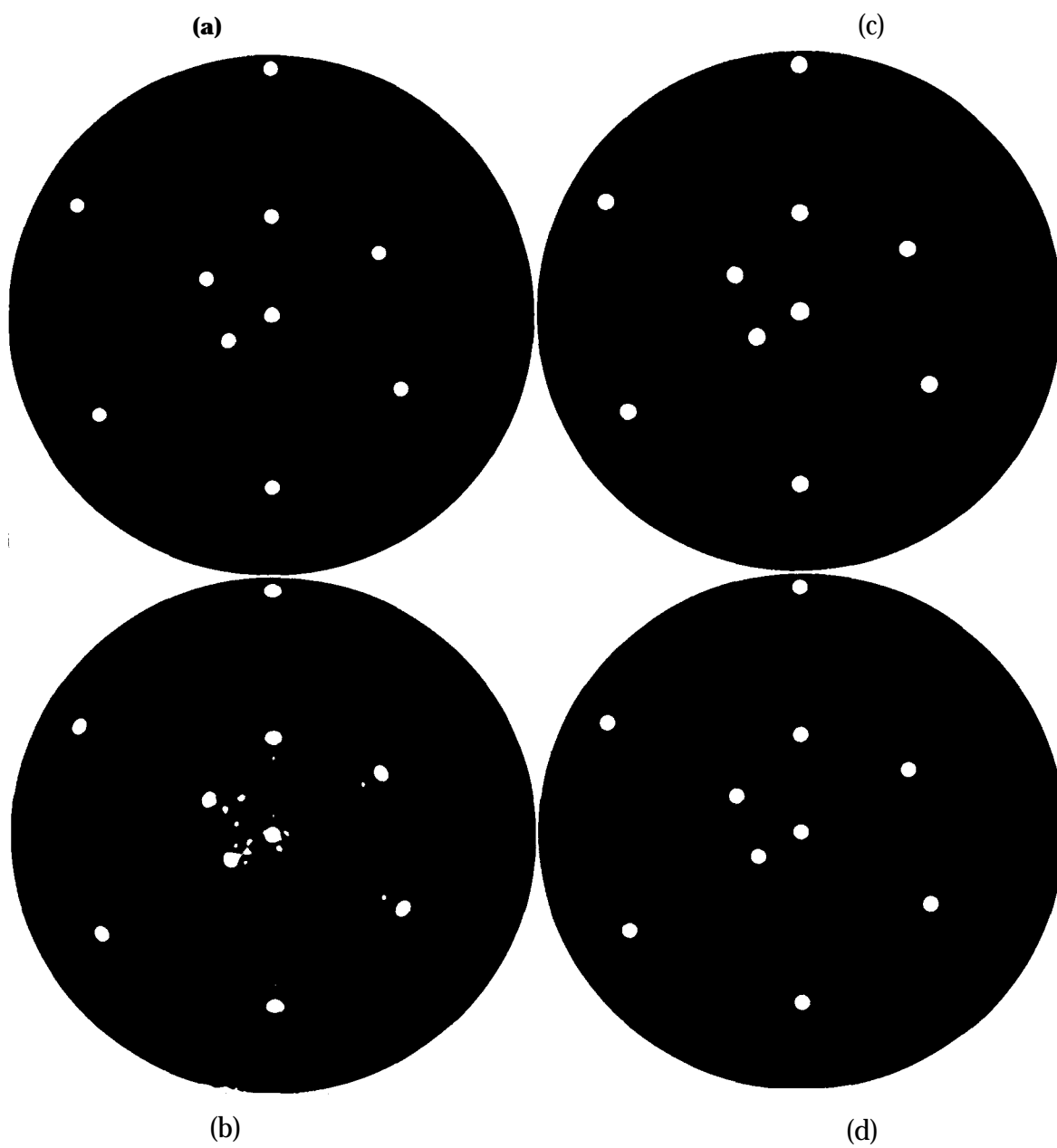


Figure 13 Simulated point spread functions of point targets of CAT parallel beam (a) $|R|$ weighting, (b) inverse filter, (c) $|R| \cdot \text{Ka}(R, 0.8)$ weighting, and (d) standard PSF form

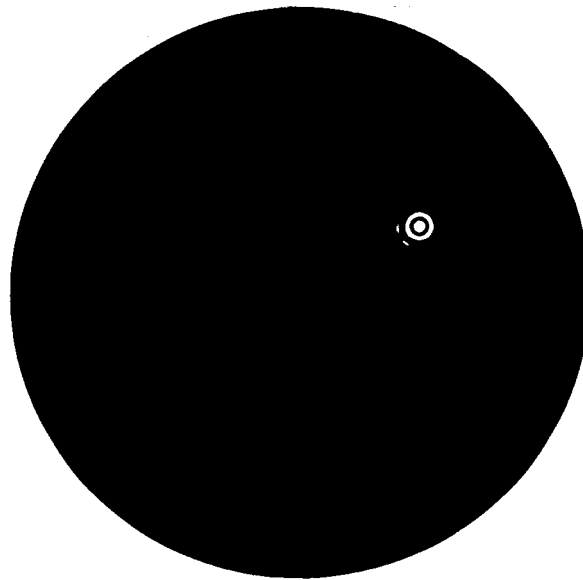


Figure 14 Simulated point spread function of point targets of HSAR with range bandwidth being .133 times of the radar center frequency

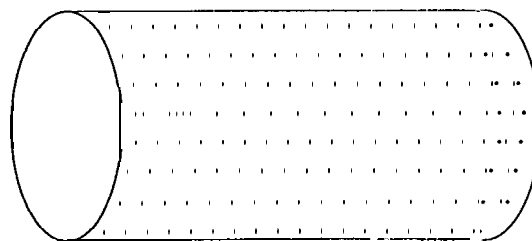


Figure 15A 3-D ultrasonic reflectivity tomography system